Journal of
Instrumentation

TECHNICAL REPORT • OPEN ACCESS

Calorimeter commissioning of the SuperNEMO Demonstrator

Published by IOP Publishing for Sissa Medialab

Received: *May 15, 2025*
Revised: *September 12, 2025*
Accepted: *October 12, 2025*
Published: *November 12, 2025*

TECHNICAL REPORT

Calorimeter commissioning of the SuperNEMO Demonstrator

The SuperNEMO collaboration

X. Aguerre,[a,b] A. Barabash,[c] A. Basharina-Freshville,[d] M. Bongrand,[e,*] Ch. Bourgeois,[e] D. Boursette,[e] D. Breton,[e] R. Breier,[f] J. Busto,[g] S. Calvez,[e] C. Cerna,[a] M. Ceschia,[d] E. Chauveau,[a] L. Dawson,[d] D. Duchesneau,[h] J.J. Evans,[i] D.V. Filosofov,[c] X. Garrido,[e] C. Girard-Carillo,[e] M. Granjon,[a] B. Guillon,[j] M. Hoballah,[e] R. Hodák,[k] J. Horkley,[m] A. Huber,[a] M.H. Hussain,[d] A. Jeremie,[h] S. Jullian,[e] J. Kaizer,[f] A.A. Klimenko,[c] O. Kochetov,[c] F. Koňařík,[k,l] S. Konovalov,[c] T. Křižák,[k,l] A. Lahaie,[a] K. Lang,[n] Y. Lemière,[j] P. Li,[b] P. Loaiza,[e] J. Maalmi,[e] M. Macko,[k] F. Mamedov,[k] C. Marquet,[a] F. Mauger,[j] A. Mendl,[k,o] A. Minotti,[h] B. Morgan,[p] I. Nemchenok,[c] M. Nomachi,[q] V. Palušová,[k] C. Patrick,[b] F. Perrot,[a] M. Petro,[f,k] A. Pin,[a] F. Piquemal,[a] P. Povinec,[f] S. Pratt,[b] M. Proga,[n] W.S. Quinn,[d] A.V. Rakhimov,[c] Y. Ramachers,[p] C. Riddle,[m] N.I. Rukhadze,[c] R. Saakyan,[d] R. Salazar,[n] J. Sedgbeer,[r] L. Simard,[e] F. Šimkovic,[f] A.A. Smolnikov,[c] S. Söldner-Rembold,[i,r] I. Štekl,[k] J. Suhonen,[s] H. Tedjditi,[g] J. Thomas,[d] V. Timkin,[c] V. Tretyak,[t,u] V. Tretyak,[c] G. Turnbull,[b] Y. Vereshchaka,[e] D. Waters[d] and V. Yumatov[c]

[a] *Université de Bordeaux, CNRS/IN2P3, LP2i, Bordeaux, UMR 5797, F-33170, Gradignan, France*
[b] *University of Edinburgh, SUPA, School of Physics and Astronomy, Edinburgh, EH9 3FD, United Kingdom*
[c] *Participant in the NEMO-3/SuperNEMO collaboration*
[d] *University College London, London, WC1E 6BT, United Kingdom*
[e] *Université Paris-Saclay, CNRS, IJCLab, F-91405, Orsay, France*
[f] *Faculty of Mathematics, Physics and Informatics, Comenius University, SK-842 48, Bratislava, Slovakia*
[g] *Aix-Marseille Université, CNRS, CPPM, F-13288 Marseille, France*
[h] *Université de Savoie, CNRS/IN2P3, LAPP, UMR 5814, F-74941 Annecy-le-Vieux, France*
[i] *University of Manchester, Manchester, M13 9PL, United Kingdom*
[j] *Université de Caen Normandie, ENSICAEN, CNRS/IN2P3, LPC Caen, UMR6534, F-14000, Caen, France*
[k] *Institute of Experimental and Applied Physics, Czech Technical University in Prague, CZ-11000 Prague, Czech Republic*
[l] *Faculty of Nuclear Sciences and Physical Engineering, Czech Technical University in Prague, Brehova, 7 115, Czech Republic*

[*] Corresponding author.

https://doi.org/10.1088/1748-0221/20/11/T11003

[m] Idaho National Laboratory, Idaho Falls, ID 83415, U.S.A.
[n] University of Texas at Austin Department of Physics, Austin, TX 78712, U.S.A.
[o] Faculty of Mathematics and Physics, Charles University, CZ-12116 Prague, Czech Republic
[p] University of Warwick, Coventry, CV4 7AL, United Kingdom
[q] Osaka University, 1-1 Machikaneyama Toyonaka, Osaka 560-0043, Japan
[r] Imperial College London, London, SW7 2BZ, United Kingdom
[s] Department of Physics, University of Jyväskylä, Jyväskylä, Finland
[t] Institute for Nuclear Research of NASU, Kyiv, 03028, Ukraine
[u] INFN, Laboratori Nazionali del Gran Sasso, 67100, Assergi (AQ), Italy

E-mail: supernemo-l@in2p3.fr

Abstract: The SuperNEMO experiment is searching for neutrinoless double-beta-decay of ^{82}Se, with the unique combination of a tracking detector and a segmented calorimeter. This feature allows us to detect the two electrons emitted in the decay and measure their individual energies and angular distribution. The SuperNEMO Demonstrator's calorimeter consists of 712 plastic scintillator blocks read out by large PMTs. Having constructed the calorimeter underground, we performed its first commissioning using γ-rays from calibration sources or from the ambient radioactivity background. This article presents quality assurance tests of the SuperNEMO Demonstrator's calorimeter, and its first time and energy calibrations with γ-rays, along with the associated methods. A time alignment of about 120 ps and a time resolution around 615 ps have been achieved. Concerning the energy, an alignment of 7.5 % has been obtained. These results will be further improved when associating the tracking detector and detecting electrons from calibration sources.

Keywords: Calorimeters; Double-beta decay detectors

ArXiv ePrint: 2412.18021

2025 JINST 20 T11003

Contents

1 Introduction

SuperNEMO is a double-beta-decay (DBD) experiment, designed to look for the hypothesized lepton-number-violating process of neutrinoless double-beta-decay ($0\nu\beta\beta$) and the Majorana nature of the neutrino.

SuperNEMO's tracker-calorimeter design, based on the technology of the NEMO-3 detector [1], allows for the study of different isotopes and tracking of the outgoing MeV-energy-scale electrons. This ability provides the means to discriminate between different underlying mechanisms of $0\nu\beta\beta$ by measuring the decay half-life and the electron angular and individual energy distributions [2]. It is also well suited for precision studies of the Standard Model two-neutrino double-beta-decay ($2\nu\beta\beta$) which is present in all $0\nu\beta\beta$ candidate isotopes [3–9]. In particular, the measurement of the full topology of $2\nu\beta\beta$ events could constrain the quenching of the axial-vector coupling constant (g_A) [10]. Adding the detection of γ-rays to the DBD events, NEMO technology can also precisely study decays to excited states of the daughter nuclei [11–13].

The basic unit of SuperNEMO is a module, as shown in figure 1. The modular design allows the detector's size to be increased by adding identical modules to the detector. The first module,

2025 JINST 20 T11003

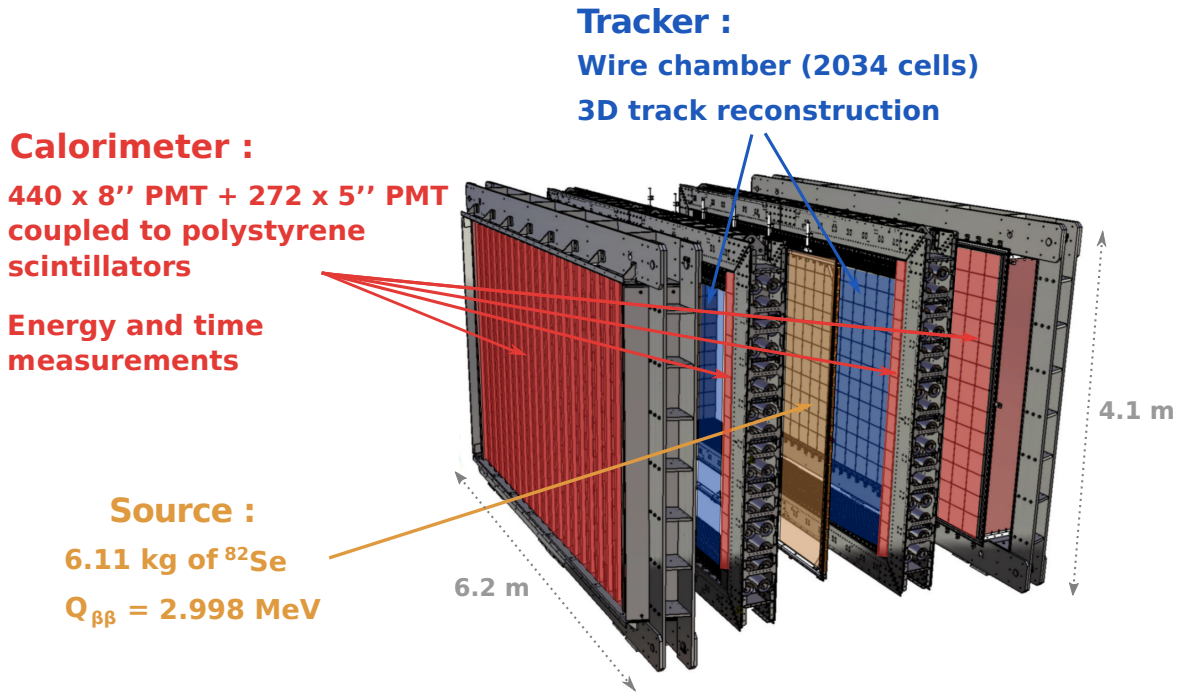

Figure 1. Split view of the sub-detectors of the SuperNEMO Demonstrator module.

named the *SuperNEMO Demonstrator*, is currently undergoing the final stages of installation and commissioning at the *Laboratoire Souterrain de Modane* (LSM), in France.

To prevent radioactive contamination from dust, a dedicated clean tent was built prior to the Demonstrator's construction. The subdetectors of the Demonstrator were successively integrated inside this clean tent. From the center to the edges, the detector consists of (see also figure 2):

- *A source frame* containing 34 isotopically-enriched DBD source foils, for a total of 6.11 kg of ^{82}Se. The source foils are 2.7 m long with a width of around 135 mm and a thickness of around 300 µm. The foils are made of purified selenium powder mixed with polyvinyl alcohol glue supported by two 12 µm-thick mylar films [14, 15]. Special care was taken in the preparation of the source foils to preserve their radiopurity, using the dedicated BiPo detector developed by the collaboration. This detector not only enabled the selection of optimal materials and procedures during the preparation phase but also allowed for systematic measurement of contamination levels prior to their installation in SuperNEMO, as detailed in [16]. At each end of the plane of selenium sources, one pure copper strip has been added as a control, to monitor the external — to the DBD source — background, in a radiopure, non-double-beta-decay sample.

- *Two tracking detectors*, made of 2034 vertical drift cells, surround the source frame. The drift cells are used to reconstruct the tracks of the β-particles emitted by the sources in three dimensions. The dimensions of one tracking volume are 3.1 m tall, 5.0 m wide and 0.44 m deep. The total tracking volume thus corresponds to about 15.4 m^3. The tracking detector gas is a mixture of 95 % helium, 1 % argon and 4 % ethanol.

- *A segmented calorimeter* consisting of plastic scintillators coupled to photomultiplier tubes (PMTs) to measure the deposited energy and the time of flight of particles coming from the

2025 JINST 20 T11003

double-beta sources or from backgrounds. Calorimeter modules surround the edges of the tracker frames, and two main calorimeter walls close the detector on each side of the tracker, parallel to the source frame. To improve the tracking-gas tightness and reduce radon penetration, a 25 µm polyamide film separates the tracker and the calorimeter.

- *The calibration tools* are comprised of an automated deployment system of radioactive sources at the top of the central frame and a light-injection system for the calorimeter blocks. The deployment system allows insertion of 42 low-activity (120–145 Bq) sources of ^{207}Bi [17] between the ^{82}Se foils, from six vessels at the top of the source frame. The calibration sources emit conversion electrons of around 500 keV and 1 MeV. They are used for regular absolute energy calibrations, on a weekly basis. In addition, a light injection system using pulsed ultra-violet (385 nm) LEDs and optical fibers, to reach the plastic scintillators, allows more regular surveys of the stability of the PMTs, several times per day. This system is accompanied by five additional reference calorimeter blocks permanently equipped with electron (^{207}Bi) and alpha (^{241}Am) radioactive sources. These are used to compare the LED pulses to calibration-source signals to monitor the LEDs.

- *A copper magnetic coil* with iron return field plates surrounds the whole detector. The 25 G magnetic field will improve the identification of the DBD electrons and enhance the background rejection (for example e^+e^- pairs or crossing electrons). The PMTs are protected from the magnetic field by pure iron shields.

- *A gas-tight anti-radon tent* is used to prevent radon from the laboratory air from entering the detector. This system is designed to reduce the radon concentration from approximately 30 Bq m^{-3} (typical laboratory air levels) to around 30 mBq m^{-3} inside the tent. To achieve this, the tent is continuously flushed with deradonized air (with a radon concentration of around 10 mBq m^{-3} [18]), produced at the LSM using an anti-radon facility. The flushing rate can reach up to 150 m^3 h^{-1}.

- *Two shielding layers*, finally, enclose the detector to reduce the background from natural radioactivity of the underground laboratory: 18 cm thick iron shielding to reduce the γ flux and 50 cm water or 24 cm polyethylene shielding to reduce the neutron flux.

The detection principle of SuperNEMO is illustrated in figure 2, with the example of a simulated two-electron event.

At the time of writing of this article, the detector itself is fully assembled at the LSM, including the magnetic coil and the anti-radon tent. The final shielding is being integrated. Once the SuperNEMO calorimeter was fully installed, with its cabling, high-voltage (HV) and front-end electronics (FEE) integrated, an early commissioning of the calorimeter was carried out. This involved measurements of γ-rays before the tracking detector was operational. This article focuses on the main-wall calorimeter, describing the commissioning methods, the initial calibrations, and presenting the preliminary performance of the calorimeter.

In this article, we present the SuperNEMO calorimeter design in section 2. We then give an overview of the preliminary tests concerning the cabling, the electronics and the PMTs in section 3. The two last sections present the timing (section 4) and energy (section 5) calibration, and performance of the calorimeter.

2025 JINST 20 T11003

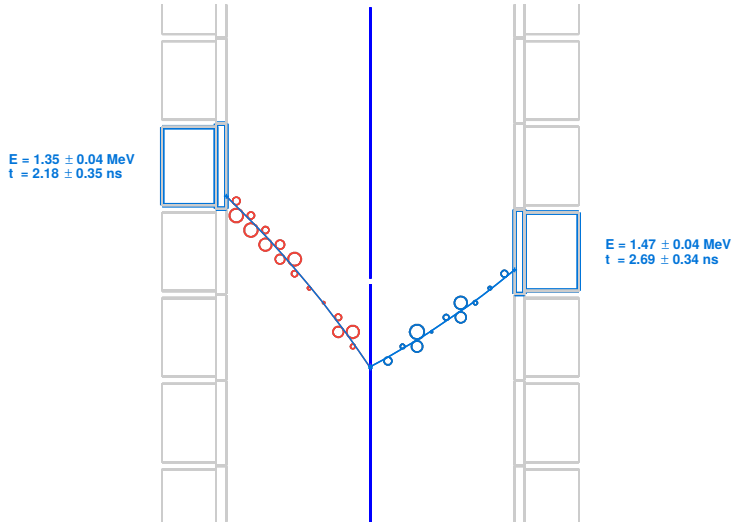

Figure 2. Top view of a simulated (with GEANT-4) DBD event illustrating the detection principle of the SuperNEMO detector. The decay electrons are emitted from the vertical isotopic source foils (in blue). The 3D tracks of the electrons are fitted from the drift cells signals (red and blue circles) of the tracking detector. Arrival time and energy of each electron can then be measured by the segmented calorimeter (grey rectangles highlighted in blue).

2 The SuperNEMO calorimeter

The SuperNEMO calorimeter is primarily dedicated to the detection of the DBD electrons emitted by the $\beta\beta$-sources. However, the detection of γ-rays is also of major importance for the study of DBD to excited states and to the identification of background events. The SuperNEMO calorimeter must therefore be efficient in gamma detection and offer a full solid-angle coverage. In total, the SuperNEMO calorimeter is segmented into 712 optical modules (OMs) to detect particles individually. The ability to measure the energy of each particle separately is a unique feature in the field of DBD experiments. An illustration of the measurement of the separate electron energies is illustrated in figure 2.

Each of the two calorimeter main walls, *M-wall*, are segmented into $20 \times 13 = 260$ OMs. Each tracking detector has $2 \times 16 = 32$ cross-wall OMs, *X-wall*, on each edge, and 16 gamma-veto OMs, *G-veto*, on the top and the bottom. The positions of these three categories of OMs are presented in figure 3.

2.1 The optical modules

One OM consists of an assembly of an organic scintillator and a photomultiplier tube glued with RTV-615 optical glue, as can be seen in figure 4. The scintillator is a polystyrene (PS)-based organic scintillator doped with 0.05 % of POPOP (1.4-bis(5-phenyloxazol-2-yl)benzene) and 1.5 % of pTP (p-Terphenyl) wavelength shifters [19, 20]. Two productions of PS scintillators have been used: a standard production and an enhanced one, which provides a better energy resolution. NUVIA CZ has enhanced the scintillator formulation in two key ways: by implementing cleaner production conditions and by optimizing the concentration of scintillating and wavelength-shifting agents [19]. Eight scintillator blocks of polyvinyltoluene (PVT), with even higher light yield, have also been included. The scintillator is wrapped with Teflon on the four lateral sides, and two layers of 6 µm aluminized mylar around all six faces (except the surface in direct contact with the PMT) to improve

2025 JINST 20 T11003

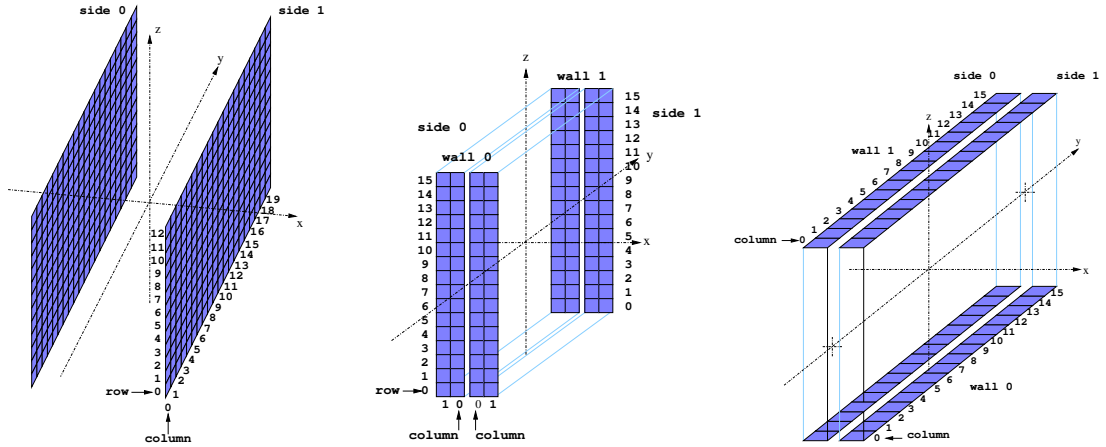

Figure 3. Illustration of the SuperNEMO calorimeter segmentation with M-wall (left), X-wall (middle) and G-veto (right) optical modules. The two sides of the detector are sometimes referred to as *French* (side 1) or *Italian* (side 0) sides, corresponding to which country of the road tunnel they are facing.

the light collection towards the PMT. The thickness of the front face of the scintillator wrapping is minimized to reduce energy losses for the entering β-particles. Two types of PMTs have been used with the scintillators: new 8-inch Hamamatsu R5912-MOD; and 5-inch Hamamatsu R6594, refurbished from the previous NEMO-3 experiment [1].

Plastic scintillators have been chosen for their excellent radiopurity, high light yield, fast time response, and low back-scattering probability for incident electrons. To investigate DBD to excited states or reject and study backgrounds, the SuperNEMO calorimeter has also been designed to detect γ-particles. The depth of the scintillators has thus been increased to almost 20 cm, while less than 3 cm would be enough to contain the DBD electrons.

As can be seen in figure 4, four types of optical modules have been used for the SuperNEMO calorimeter.

The configuration of OMs in the SuperNEMO calorimeter has been chosen to optimise our energy resolution when detecting DBD electrons, which will be mostly detected on the two main calorimeter walls, while also fitting the constraints of the tracker's mechanical design. The M-wall OMs are made of the best plastic scintillators with 8-inch PMTs, to achieve 8 % FWHM energy resolution at 1 MeV, except for the top and bottom rows, where 5-inch PMTs are used, since the end-caps of the tracking cells prevent the β-particles emitted from the DBD sources from being detected there. To reach the best energy resolution and light-collection uniformity possible, large-photocathode-area PMTs are glued directly to these M-wall scintillators, without interface light guides. These scintillators also have a 31 mm step, providing a larger surface area compared to the rest of the block (steps visible in figure 4) to maximize the detection surface and to leave space for the magnetic shield surrounding all the M-wall OMs. On the small sides of the trackers, parallel to the tracking cells, the X-walls are made of smaller scintillators coupled to 5-inch PMTs with a PMMA light-guide. A cylindrical mu-metal magnetic shield covers the PMT and its light guide; as the PMT is small, it is unnecessary to shield the scintillator. These X-wall OMs can also detect DBD particles from the source foils, but with a poorer energy resolution of 12 % FWHM at 1 MeV. A similar design is used for the G-veto OMs, which are installed on the top and bottom of the trackers, but with larger scintillator blocks.

2025 JINST 20 T11003

Similarly to the top and the bottom OMs of the M-wall, these OMs will not detect the β-particles of the sources because they are placed above or below the end-cap of the tracking cells. The constraint on the energy resolution can be relaxed and they achieve 16 % FWHM at 1 MeV. More details about the development of these optical modules and the radiopurity budget can be found in [19].

Figure 4. Picture of the four types of optical modules used for the SuperNEMO calorimeter during assembly. From left to right: two M-wall OMs with 8- and 5-inch PMTs, one X-wall OM and one G-veto OM with 5-inch PMTs and PMMA light-guide. Notice the wider step in the M-Wall scintillator block's shape at the bottom of the corresponding OM. Scintillators and light-guides are wrapped with aluminized mylar.

To ensure the radiopurity of the SuperNEMO calorimeter, the components of the OMs have been carefully selected using high-purity germanium (HPGe) detectors. The glass of the PMTs (650 g) and their electrical insulators (25 g) represent the major contribution to the radionuclide activities of the OMs. For the 8-inch Hamamatsu PMTs, contamination levels of 0.95 Bq/PMT in ^{40}K, 0.62 Bq/PMT in ^{214}Bi and 0.26 Bq/PMT in ^{208}Tl have been measured. Only upper limits of a few mBq/kg for the three main radionuclides have been set on the radiopurity of the plastic scintillators.

2.2 The main wall calorimeter frame

The dimensions of the calorimeter frame have been driven by the source surface to offer an active area of about $5 \times 3\,\mathrm{m}^2$. It would be difficult to transport a detector of this size to the Laboratoire Souterrain de Modane (LSM) in one piece. Furthermore, these dimensions could not fit through the LSM's entrance from the tunnel. The frame was therefore designed as an assembly of four beams to be assembled underground, and to be populated with the optical modules onsite. The structure of the calorimeter frame has to support the weight of 260 OMs that make up each main wall, each weighting around 25 kg, and totaling about 6.5 tons. The four beams consist of reinforced structures made from 30 mm-thick pure iron plates. This material has been selected for mechanical considerations, and for its very good radiopurity.

Because of the fragility of the scintillator wrapping, and to speed up the integration process underground, the OMs were packed into so-called *calobricks*. These calobricks were horizontal assemblies of 4×2 or 4×1 OMs, as shown in figure 5. The support structure of the calobricks relies on the iron magnetic shields, which are screwed together with radiopure brass bolts and separated by PMMA spacers. The OMs are attached to the transverse plate of the magnetic shield by nylon screws. The magnetic shields have been developed to protect the PMTs from the 25 G magnetic

2025 JINST 20 T11003

field, needed in the tracker for electron-positron separation via the curvature of their tracks. They consist of 3 mm-thick ARMCO pure iron plates, cut and soldered by laser, to prevent contamination. This material was preferred to mu-metal because of its better radiopurity (only upper limits at 90 % C.L. have been measured at the level of 5.7 mBq/kg in ^{40}K, 1.1 mBq/kg in ^{214}Bi and 0.48 mBq/kg in ^{208}Tl). Special annealing treatment was used to improve the magnetic properties of the shields after production. The shields cover a large part of the scintillator because the need to go beyond the PMT photocathode has been demonstrated, to reduce the penetrating magnetic field. There is, however, a residual magnetic field that still penetrates the PMT, of the order of 1 G. In the end, only a few percent loss has been observed on the PMT charge, which could be compensated for by a moderate increase in the high voltage, on the order of 20 V [21].

Figure 5. Picture of a calobrick of 2×4 OMs during insertion of the pure iron magnetic shields.

2.3 The calorimeter cabling

The SuperNEMO detector is protected by an air-tight anti-radon tent flushed with radon-free air. The calorimeter electronics are outside of this tent; the HV and signal cables, connecting the PMTs to the electronics, have to go through the tent while maintaining the gas tightness. For this reason, different sets of cables are used inside (see figure 6) and outside of the anti-radon tent. Internal and external cables are connected together at the patch panels on the anti-radon tent with dedicated connectors. The patch panels are made of drilled pure-iron plates to accept, from inside, fixed female connectors and, from outside, removable cables with their male connectors.

Signal cabling

The SuperNEMO calorimeter's signal cables were selected based on their radiopurity, compatibility with the front-end electronics, and a balanced compromise between signal quality, cable weight (to minimize the amount of material inside shielding), and cost. It is a coaxial cable with the reference M17/93 RG-178 from the Axon company, with a transparent sheath that provides a better radiopurity.

2025 JINST 20 T11003

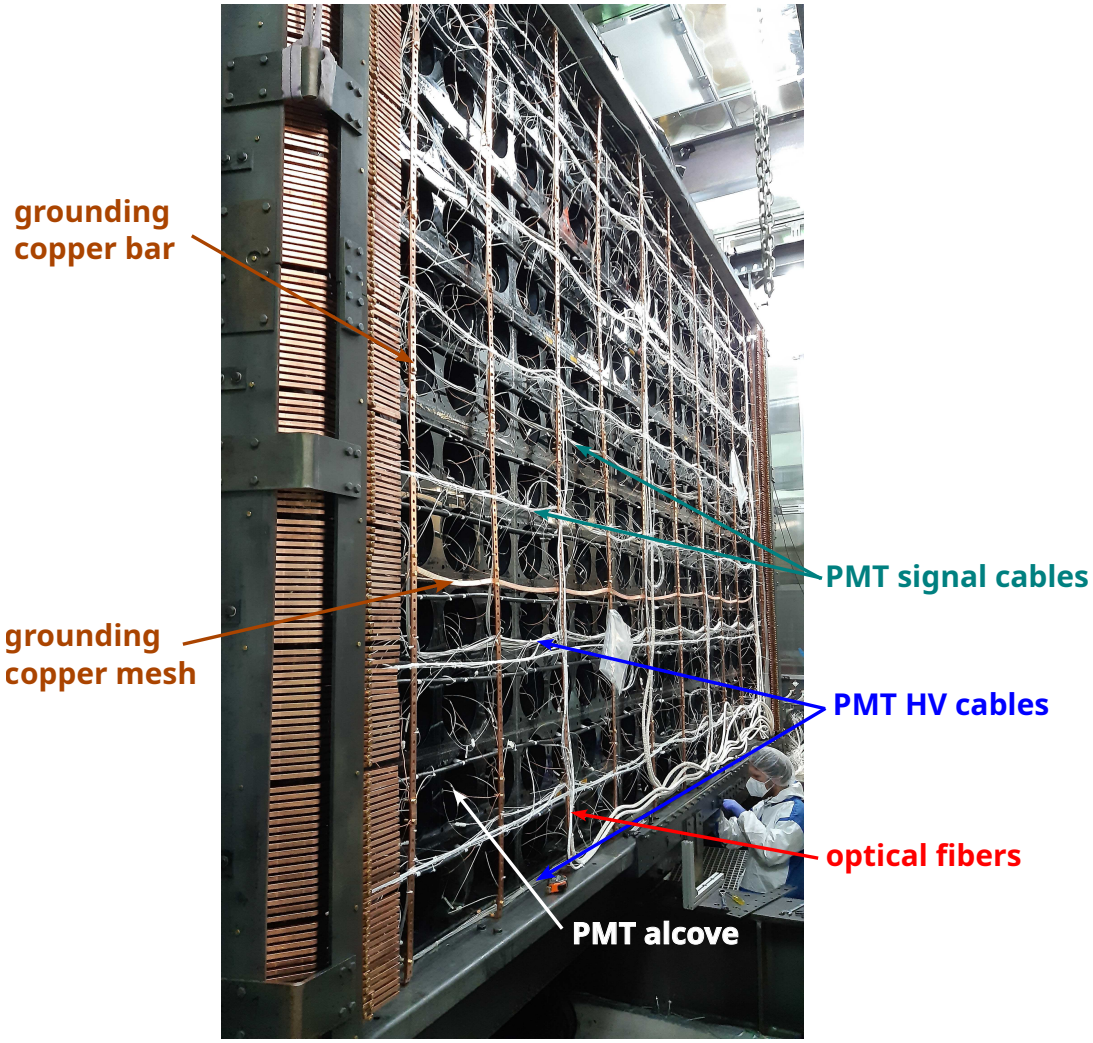

Figure 6. Picture of the back of one calorimeter main wall showing the horizontal routing of the signal and HV cables to the PMT dividers in the alcoves, the vertical grounding copper bars, the large and small copper braids and the optical fibers of the light injection system in their white jackets.

Only the contamination in ^{40}K has been measured, at $(25 \pm 4)\,\mathrm{mBq\,kg^{-1}}$; 90 % C.L. upper limits have been set at $1.1\,\mathrm{mBq\,kg^{-1}}$ in ^{214}Bi and $0.36\,\mathrm{mBq\,kg^{-1}}$ in ^{208}Tl. In order to reduce the amount of cables inside the anti-radon tent, the cables have been cut to the required lengths to reach each PMT by first a vertical routing to the OM's row, and then a horizontal routing to the PMT's location. The cables are fastened to vertical copper bars attached to the calorimeter's pure-iron frame. This scheme allows the mapping of the OMs in the detector to be reflected at the patch panel and at the front-end electronics boards (see section 2.5). The separation between two adjacent OMs are 25 cm between OMs in both directions. This results in internal signal cables with lengths ranging from 3.25 m to 11 m. The difference in cable lengths is compensated for offline by time alignment of all the channels, as described in section 4. The cables are connected to the PMT dividers using two female Souriau pins (SC20WL3S25) for the inner connector. The other end of the internal signal cable has a female MCX coaxial connector (MP-27-10M TGG) straight bulkhead jack to be fixed on

2025 JINST 20 T11003

the patch-panel plate. We have opted for the most straightforward solution to connect the internal and external cables. This configuration ensures connection quality equivalent to that at the front-end electronics, where detailed studies have already been conducted.

Given the relatively small dimensions of the patch panel and the compactness of the front-end electronics, all the external cables have been cut to the same length of 7 m. For simplicity, the same Axon cable has been used as for the internal cables. On the SuperNEMO front-end boards (section 2.5), a female MCX 50 Ohms coaxial connector is used, similar to that used at the patch panel for the internal cable. Thus, the external signal cables have male coaxial MCX connectors from Radiall on both ends.

HV cabling

For the same reasons as for the signal cables, the HV cables are divided into internal and external cables at the anti-radon tent. Power for the SuperNEMO calorimeter is supplied by three CAEN SY4527 units. The crates are populated with 32-channel A1536 HV boards. These boards come with 52-pin connectors from Radiall. To fit with this connector, an HV cable produced by CERN was selected for the external part. It consists of a 37 multi-cables bundled in a red jacket. In this cable, 32 channels are used to supply HV to the individual PMTs, and 5 channels are used to provide grounding. The connectors on this external HV cable are a Radiall connector (691802002) at the electronics side, and Redel LEMO 51-pin straight plug (SAG.H51.LLZBG) at the patch-panel side.

Inside the anti-radon tent, the HV cables become individual coaxial cables. The connector at the patch panel is a fixed-socket Redel LEMO (SLG.H51.LLZG) corresponding to the female external one. An in-house circuit has been designed to merge the grounds at this level, and distribute all the HV to the dedicated pins of the connector to the individual internal cables. The internal cable is an Axon AK4902A coaxial HV cable, also selected for its good radiopurity. Contamination levels in ^{40}K and ^{214}Bi have been measured at $(23 \pm 4)\,\mathrm{mBq\,kg^{-1}}$ and $(1.1 \pm 0.3)\,\mathrm{mBq\,kg^{-1}}$ respectively, while a 90 % C.L. upper limit has been set to $0.3\,\mathrm{mBq\,kg^{-1}}$ in ^{208}Tl. Similarly to the signal cable, the external HV cable can be disconnected from the outside, while the internal one is fixed to the patch panel. The internal cables are connected to the PMT dividers using two Souriau pins (one male SM20WL3S26 for the core, and one female SC20WL3S25 for the ground mesh, to prevent misconnection). A small copper braid has also been added to connect the PMT divider to the mechanical grounding of the calorimeter wall.

The routing scheme of the internal cables on the calorimeter is similar to the signal cables, but with a different pattern, to fit the mapping between OMs and the channels on the HV boards: see section 2.5. We have also avoided routing signal and HV cables together, to reduce possible noise or cross-talk.

2.4 Electrical grounding

In order to prevent noise being induced on the signal channels and electric charge accumulation in the detector, special care has been taken to ground the SuperNEMO calorimeter. Two types of copper braids have been deployed to ensure this grounding. Firstly, a large copper braid ($10\,\mathrm{mm^2}$) is routed all along the calorimeter walls (see figure 6) and connected to the vertical copper bars also used to support the PMT cables. The connection is made by pinching the copper braid with a copper plate on the vertical bars. To connect each PMT divider to ground, a second copper braid has been added ($1.5\,\mathrm{mm^2}$). It is soldered to the naked ground mesh of each HV cable and then pinched to the large copper braid with small copper plates.

2025 JINST 20 T11003

The whole detector and its electronics are installed on brass plates that ensure the overall grounding of the experiment. These brass plates are connected to the general grounding of the LSM. All the apparatus, sub-detectors and patch-panels have been grounded to these plates through copper plates or braids.

2.5 Calorimeter electronics

The SuperNEMO electronics are installed fully outside the detector and its shielding. All the electronic components are grouped inside six electronics racks. Two racks are dedicated to the calibration systems, two others to the calorimeter, and two more to the tracker. CAEN systems provide the high voltage (HV) to the PMTs. Custom-made front-end boards (FEB) digitize the signals [22]. These FEBs are inserted inside *versa module eurocard* (VME) crates with a custom backplane developed for the experiment. The FEBs are handled by a control board (CB) in each VME crate. The CBs ensure the synchronization of the FEBs, exchange the trigger decisions, and concentrate and transmit the signals registered by the FEBs. Both calorimeter and tracker electronics are managed by a single trigger board (TB) connected to all the CBs and the DAQ. The TB distributes the 40 MHz clock (25 ns clock tick) and takes the triggering decision, which is configurable. A complete description of the SuperNEMO electronics can be found in [23]. One of the racks also includes the computers for DAQ, data storage, and a switch for network distribution. The collected data is transferred daily to CC-IN2P3[1] for storage, processing and analysis.

The SuperNEMO trigger system is designed to select only events of physical interest and reject spurious events (self-triggering of the drift cells or PMTs) in order to reduce the global acquisition rate. At each clock tick (25 ns), the trigger system collects and merges the 712 calorimeter channels' statuses (triggered/not triggered) based on an optimized signal-amplitude threshold per channel. A column of PMTs (13 PMTs for main walls, or 16 PMTs for X-walls and G-vetos) is connected to a single calorimeter FEB. Each FEB builds a trigger-primitive bitset which is sent to the dedicated CB each 25 ns. Constrained by the bandwidth from the FEBs to the CB, this bitset is limited to 5 bits. The trigger-primitive bitset is composed of a threshold multiplicity at the level of the FEB. At each clock tick, the CBs collect the trigger-primitive bitset from the connected FEBs (20×5 bits from each main wall and 12×5q bits from all of the X-walls and G-vetos). Each CB produces a crate trigger bitset of 18 bits. The bitset is composed of: a threshold multiplicity at the level of the crate (from 0 to >3) and 10 bits called the *zoning word*. Each bit of this zoning word can be activated in case of hits in the corresponding geographical location of the detector. Three crate trigger bitsets from the calorimeter crates are uploaded to the TB. This strategy enables a check for coincidence between tracks from the tracker and hits from PMTs, in time and space.

The PMT pulses are digitized in the FEBs at a sampling rate of 2.56 GS/s over 1024 samples, providing a total time window of 400 ns. The calorimeter data are described by a header and the data itself. The header is composed of: the trigger ID, the electronic channel address and the timestamp, which is the absolute time of the experiment tagging the last sample encoded by the 48-bit TDC counter provided with a 160 MHz clock by the SAMLONG chip (390.625 ps steps), which is the heart of the calorimeter FEBs. The data contain the metadata computed by the SAMLONG chip [24] and the digitized samples of a pair of detector channels connected to the chip. The recorded digitized waveforms are 1024 values of ADC encoded in 12 bits, corresponding to the 1 V input range of the chip (0.25 mV steps). The metadata includes a raw estimation of the signal baseline, a charge, a peak amplitude and values at specific times along the waveform.

[1] https://cc.in2p3.fr/en/.

2025 JINST 20 T11003

In order to refine the calculation of these parameters for the determination of the physics variables of interest in each event, offline pulse-shape analysis algorithms have been developed on the SuperNEMO PMT signals. Four parameters of major interest are computed for each PMT pulse: *baseline, amplitude, time* and *charge*. An illustration of the computation of these parameters on an 8″ PMT signal of the SuperNEMO calorimeter is presented on figure 7. The use of a constant fraction discriminator (CFD) is independent of the amplitude of the pulses in order to improve the precision on the time measurement, compared to NEMO-3 where time-amplitude corrections were used.

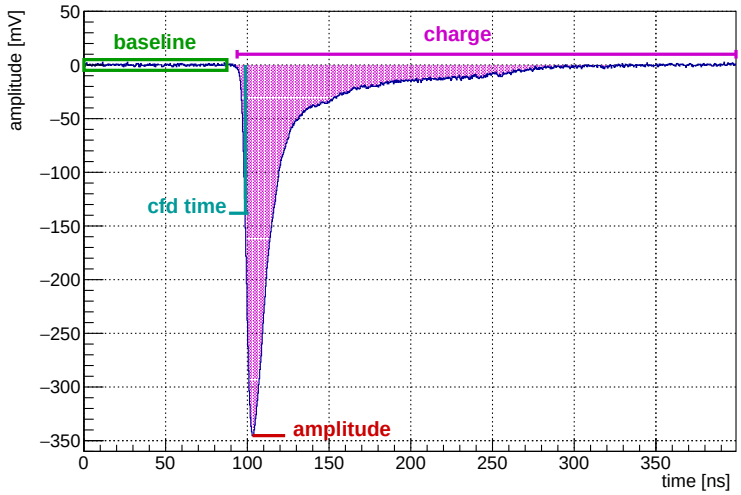

Figure 7. Example of an 8″ PMT pulse digitized by the SuperNEMO front-end electronics at 2.56 GS/s, illustrating the offline reconstructed parameters for the analyses. The baseline is computed by averaging the noise over the samples before the pulse [25]. The pulse amplitude corresponds to the minimal sample of the waveform. The time of the pulse is computed by a constant fraction discriminator (CFD) at 40 % of the amplitude. Finally, the charge is the integration of the pulse over the time window after the baseline. All the parameters for these computations can be adjusted.

3 Calorimeter preliminary tests

After the detector closure and the cabling operations on the calorimeter, the front-end electronics were installed, so that calorimeter-commissioning data could be taken. The first stage of the calorimeter commissioning consisted of testing the whole cabling network, before investigating the PMT signals and determining the performance of the calorimeter.

3.1 HV cabling tests

The test of the HV cables was performed by a basic method: progressively increasing the voltages applied to each PMT to their nominal values (around 1500 V). After fixing minor issues, the HV delivery system of the SuperNEMO calorimeter was fully operational.

This required the detector to be covered with black plastic light protection and for the light to be switched off in the LSM, since the detector was not light-tight at this stage of integration. In order to avoid this operation, and to preserve access to each OM, an alternative method was used to test the signal cabling, as described below.

2025 JINST 20 T11003

3.2 Signal cabling quality with reflectometry measurements

The first quality-assurance tests performed on the signal cabling were possible without switching on the PMTs, thus avoiding the need to cover the whole detector for light tightness. For the very first tests, a powerful feature of the SuperNEMO front-end electronics was exploited. On each board, it is possible to generate an electronic signal, with a gate shape, which is injected into each signal channel. These pulses are then transmitted through the coaxial signal cables to the PMT dividers, where they are then reflected by the RC circuit back to the electronics. This feature allows us to test the whole chain of signal transmission and its quality. We called these measurements *reflectometry*.

Thanks to the 400 ns length of the sampling window and the maximum cable length of about 18 m, both the generated and the reflected pulses can be digitized and stored in the same waveform. An example of such a waveform for one FEB with 13 channels is shown in figure 8. We can see the first generated pulses around 100 ns and the reflected pulses starting after 200 ns. Concerning the reflected pulses, we observe three features:

- There is a few-nanosecond time shift between the reflected pulses. This is due to the increasing cable length. The routing of the signal cables is made up of rows of two, one above and one below the cable. The cable lengths are separated by approximately 50 cm. This is why the reflected pulses come in pairs, except for the 13^{th}, which is alone.
- The reflected pulse shapes vary with the increasing cable length. We observe an attenuation in amplitude, which is accompanied by a broadening of the pulses.
- Two different shapes of reflected pulses can be seen, corresponding to the 5- and 8-inch PMTs. The first and the last pulses, corresponding to the 5-inch PMTs, present a wave-like shape. The others, corresponding to the 8-inch PMTs, are closer to a gate signal. This can be explained by the difference in the decoupling resistances on the PMT dividers, which are 1 MΩ and 10 kΩ for the 5-inch and 8-inch PMTs, respectively.

The analysis of the reflectometry data allowed us to perform a visual inspection of the reflected pulses. Firstly, we needed to check if the time position of each reflected pulse was correct. For example, we detected issues at the patch panel when the pulses were reflected at a shorter time than expected. We could also spot wrong cable lengths in this way. Secondly, the shape of the reflected pulses allowed us to investigate connection defects or damage to the connectors or the PMT dividers. All these minor defects were easily corrected. The reflectometry measurements provided an efficient quality check of the calorimeter's signal cabling, and allowed us to have fully-operational signal cabling.

3.3 PMT signal verification

In order to continue with the tests of the calorimeter signal cabling, we profited from the PMT signals. First, we switched on the PMTs one by one and checked, through the acquisition, whether the correct channel was triggering and showing PMT pulses. This test also allowed us to validate the correspondence between HV and FEB channels. Secondly, a visual inspection of the PMT pulses helped to find more problematic channels. A few problematic channels revealed some broken PMTs. These were confirmed by looking from the back of the PMT, where the normal yellowish color of the PMT was gone. This means the photocathode had disappeared because of a broken vacuum. This damage might have been caused by a shock on the PMT, or by too much stress on the pins exiting

2025 JINST 20 T11003

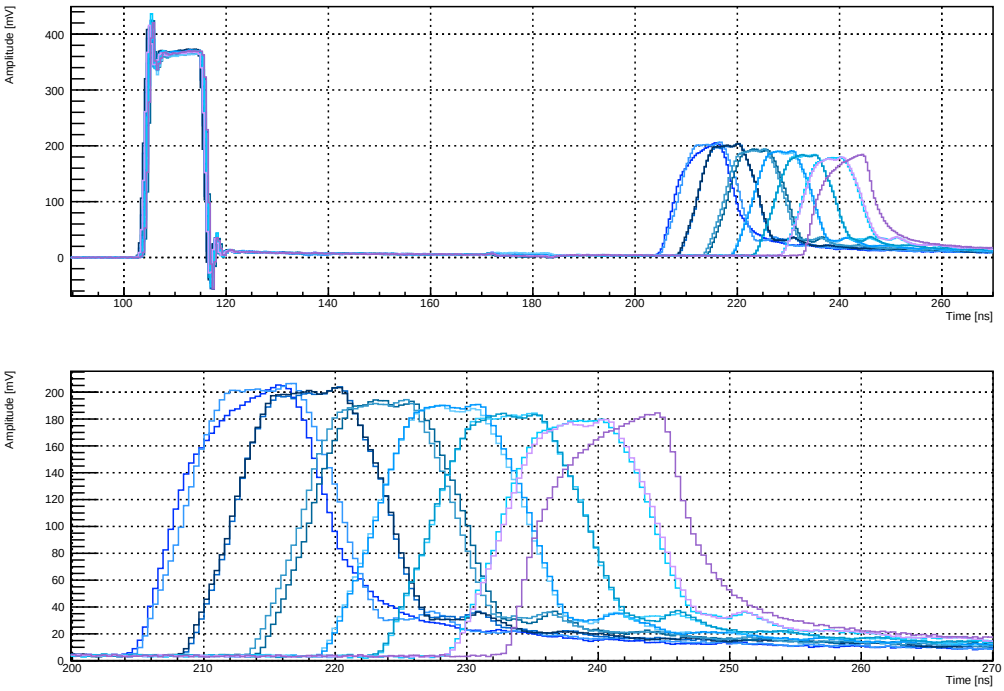

Figure 8. (top) Reflectometry example of the averaged waveforms of the 13 channels of one front-end board. The generated pulses can be seen around 105 ns and the reflected pulses starting from 205 ns. The time shift and the attenuation of reflected pulses are explained by increasing cable lengths. (bottom) Zoom on the reflected pulses. The two wave-like shapes (the first and last pulses) correspond to the top and bottom 5-inch PMTs, whereas the others are coming from 8-inch PMTs.

the glass. Since the PMTs were tested at LSM just before integration on the wall, damage certainly occurred during the screwing-together of the calobricks. A summary of the non-functioning PMTs can be seen in figure 9. In total, 16 out of 712 PMTs are non-operational, which represents a dead-channel rate around 2 %. The most critical area of the main walls — highlighted in green in the figure 9 — covers 3 % of the Italian-side wall and 1 % of the French-side wall. In the worst-case scenario, this could result in a 6 % loss in detection efficiency for double beta decay electrons. To accurately quantify this potential loss, a dedicated Monte Carlo study is foreseen.

4 Time calibration of the calorimeter

The goal of the time calibration is to compensate for all relative timing differences between any two channels of the SuperNEMO calorimeter. These time differences can be due to different cable lengths; to light collection in the scintillator; or to the PMT transit time, which depends on the HV. To a minor extent, it can also be due to the collection of signals in the backplane of the front-end electronics crates.

4.1 Reflectometry time measurements

The amount of cables inside the anti-radon tent has been minimized in order to reduce the radioactive background. Thus, the PMT cables have been cut to the exact lengths to reach the PMTs from the patch panel. This causes time delays between the different channels of the segmented calorimeter,

2025 JINST 20 T11003

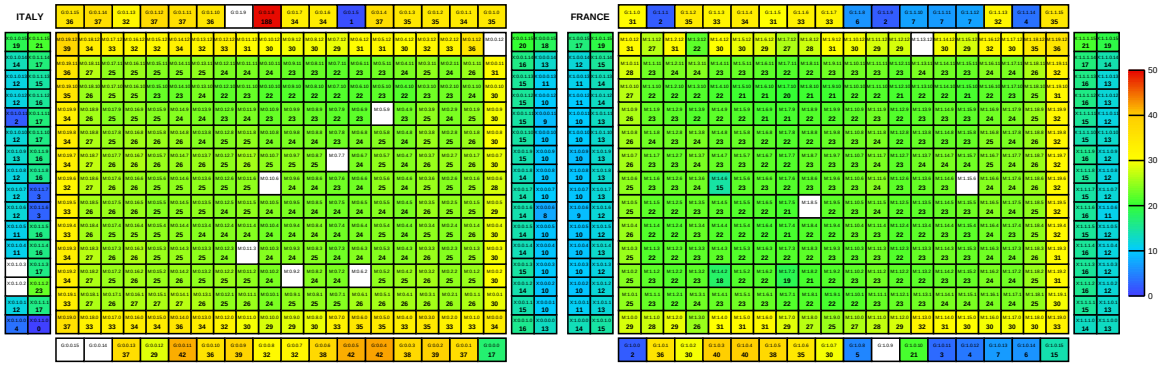

Figure 9. Illustration of the functioning PMTs of the SuperNEMO calorimeter, as of Summer 2023, without detector shielding. The picture represents the count rate per minute (indicated by bold numbers and color map) of γ-like events, for the two sides of the detector (Italy and France). The white boxes correspond to disconnected cables at the time of the measurement or dead PMTs. Some low-gain G-veto OMs also appear at the top and bottom, but have been recovered later.

which need to be calibrated. In SuperNEMO, the timing performance is of major importance. In particular, time coincidences are needed to select the two electrons originating from the source foil, and to reject crossing electrons, which are external background events produced by γ-rays. This can be done thanks to a time-of-flight analysis.

The reflectometry technique, presented in section 3.2, also provides an efficient way to measure the time differences between all of the channels. The analysis of the waveforms was exploited to measure the time difference between the generated and reflected pulses for each channel, which would correspond to twice the time delay for PMT signals. All the time differences were measured for the 712 channels thanks to this technique. Figure 10 shows the result for the main wall OMs. We can observe the regular increase in cable lengths for the two main walls, from the patch-panel corner in the bottom to the opposite top corner, which results in an increase in the time differences.

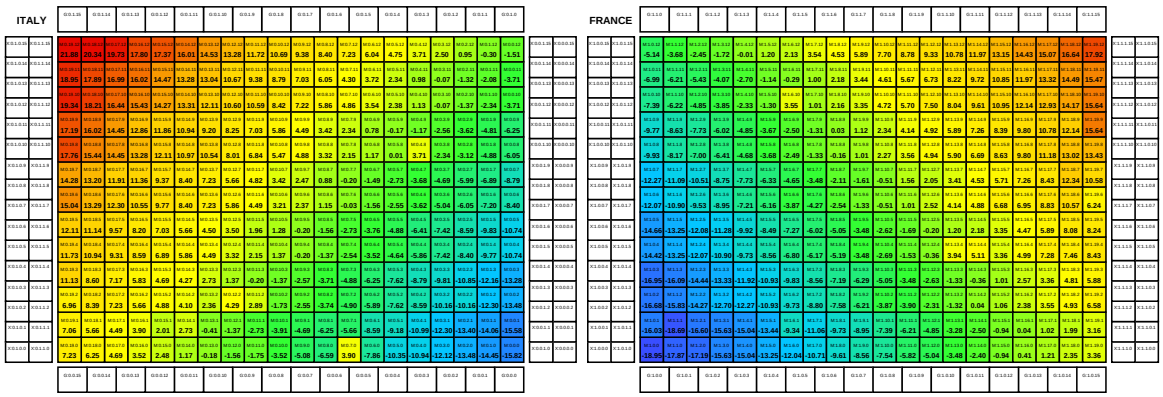

Figure 10. Half-time difference measurements in ns (indicated by bold numbers and color map) between the generated and reflected pulses in reflectometry runs, for the two calorimeter main walls [26]. Some cables have slightly different lengths than expected; they appear in different colors to their neighbours. The tiny text references correspond to the identification of the OMs.

2025 JINST 20 T11003

4.2 Time calibration with ^{60}Co source

A ^{60}Co source is very well suited for performing a time alignment of several detectors. It emits two γ-rays within a very short time coincidence (< 1 ps), with 1.17 and 1.33 MeV energies. Comparing the time measurements of these two gammas detected in two different OMs would integrate all the processes (electronics, instrumental and physics) that could produce time delay or jitter in the time measurement. Following the reflectometry measurements, this method was used to perform a complete time calibration of the SuperNEMO calorimeter and, subsequently, to study its time resolution. The source was placed about one meter away from a main calorimeter wall, with nine positions used for each main wall. The measured time t_i^{meas} of a calorimeter hit i can be written as:

$$t_i^{\text{meas}} = \text{ToF}_i + \kappa_i \tag{4.1}$$

where κ_i is the time calibration constant to be determined for each OM i and ToF_i is the time-of-flight of the gamma particle from the source to the hit calorimeter i. The time difference between two OMs, $\Delta t_{ij} = t_j^{\text{meas}} - t_i^{\text{meas}}$, will provide the difference between the calibration constants κ by:

$$\kappa_j - \kappa_i = \text{ToF}_i - \text{ToF}_j + \Delta t_{ij} \tag{4.2}$$

The difference of time of flight $\text{ToF}_j - \text{ToF}_i$ is easily calculated from the distance traveled by each γ-particle from the position of the ^{60}Co source to the interaction point in the calorimeter. This interaction point is unknown and we assume the γ-particle interacted in the middle of the scintillator. Given the results presented here, the choice of this reference does not appear to affect the analysis, as only the relative difference between the two times is considered. This choice could be refined in future analyses. The time difference distributions Δt_{ij} are then fitted by a Gaussian function. The fitted mean value is used to determine the calibration constants, and the fitted standard deviation to determine the uncertainty. As the coincident-gamma rate decreases when the distance between two OMs increases, the calibration procedure has to be limited to neighboring OMs then iterated. Therefore the error on the calibration constant for an OM at the edge of the wall is higher.

By convention, we define a reference OM with $\kappa_{\text{ref}} = 0$ ns, to which all other OMs will be relatively calibrated. Each M-Wall has one reference OM located at its center. The result of this process for all the M-wall OMs is presented in figure 11. The values have also been computed for the X-wall and G-veto blocks, but are not presented here.

We recognize the pattern dominated by the cable lengths, as in figure 10. It confirms that the other effects are lower-order corrections to the time delay. The statistical uncertainties on these calibration constants present a peaked distribution around 30 ps for each of the M-walls, with a standard deviation around 20 ps. However, there are several uncertainty values extending up to ~100 ps, for OMs at the edge of the wall, which will require more statistics or further studies. Some systematic studies were performed to test the validity of the results by varying selection criteria in the analysis, and the results were found to be stable [27].

In order to verify these results, a comparison with the reflectometry measurements was performed. Good correlation was observed since the difference between the calibration constants is below one nanosecond. The dispersion is, however, larger since a standard deviation of about 2 ns has been found. The reasons for these differences are understood, because the ^{60}Co measurements also include time jitters (difference in transit times, transit time spread) introduced by the PMTs.

2025 JINST 20 T11003

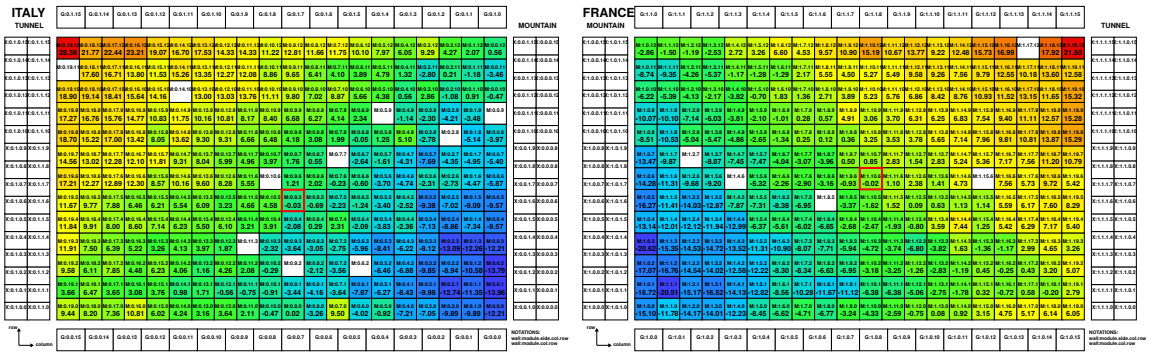

Figure 11. Time difference in ns (indicated by bold numbers and color map) to the central OM of each wall, with the ^{60}Co data, determining the relative calibration constants κ_i for the two calorimeter main walls. The two red squares represent the two central reference OMs. The white boxes correspond to dead PMTs or issues in calibrating a specific OM with these data. Reproduced from [27].

After applying the calibration constants to the time measurements, a final verification consisted of checking the time-of-flight (ToF) alignment of the two γ's emitted from the ^{60}Co source. The distribution of the ToF differences between the two OMs is well centered at zero [27]. The standard deviations are about 120 ps for the M-wall. The choice of a reference OM with the best time resolution in the M-wall could improve the precision of the calibration for all the OMs. Nevertheless, these results are quite impressive given the status of the detector in this early commissioning.

4.3 Determination of the calorimeter time resolution with ^{60}Co source

After the alignment of the calorimeter OMs, we can measure the time resolution of each OM. This will be decisive for the quality of the ToF analysis, which is based on a χ^2 comparison with a formula of the type $\chi^2 = (\Delta t)^2/\sigma_t^2$, where Δt is the time difference between the registration of signals from two OMs and σ_t the coincidence time resolution of the calorimeter, see for example [28]. The objective is to be comparable to NEMO-3, for which $\sigma_t = 660$ ps has been measured with 1 MeV γ-rays [29], despite the fact that SuperNEMO scintillators blocks are larger.

In order to determine the individual time resolution of each OM, a new method has been developed. The uncertainties on the time difference measurements, denoted σ_{ij}, represent a combination of the time resolution σ_i for the OM i and σ_j for the OM j:

$$\sigma_{ij}^2 = \frac{\sigma_i^2}{E_{ij}} + \frac{\sigma_j^2}{E_{ji}} \tag{4.3}$$

where E_{ij} corresponds to the energy measured by the OM i in the events in coincidence with the OM j, and E_{ji} the opposite. Energies must be taken into account since the time precision depends on the number of detected photons, and thus on the energy. In order to determine the individual time resolutions σ_i, we can triangulate between three OMs and use the measurements for the pairs ij, jk and ik. Solving the system of three equations allows us to determine the three resolutions of interest. Repeating these calculations allows us to get the individual resolutions for all the OMs of the SuperNEMO calorimeter. The results of this method for the M-wall OMs are presented in form of maps in figure 12. The time resolutions are quite uniform around 615 ps, except for the top and bottom rows, which show poorer time resolution since the 5-inch PMTs of these OMs collect less light.

2025 JINST 20 T11003

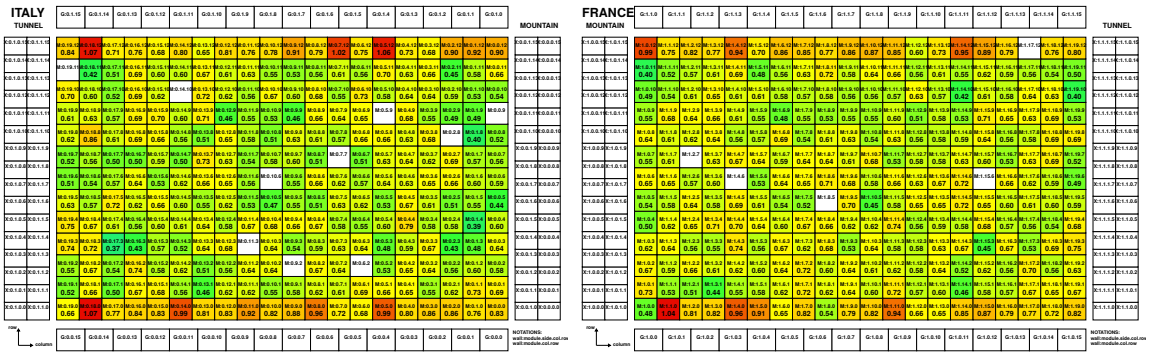

Figure 12. Time resolutions σ_t in ns (indicated by bold numbers and color map) of each OM of the two calorimeter main walls obtained with the ^{60}Co calibration source. The white boxes correspond to dead PMTs or issues in calibrating a specific OM with these data. Reproduced from [27].

Similar maps were generated for the uncertainties on the time resolution for each OM [27]. These maps revealed larger uncertainties at the edges of the detector, which could be improved with higher collected statistics. The final one-dimensional distributions of the time resolutions and the corresponding uncertainties are presented in figure 13.

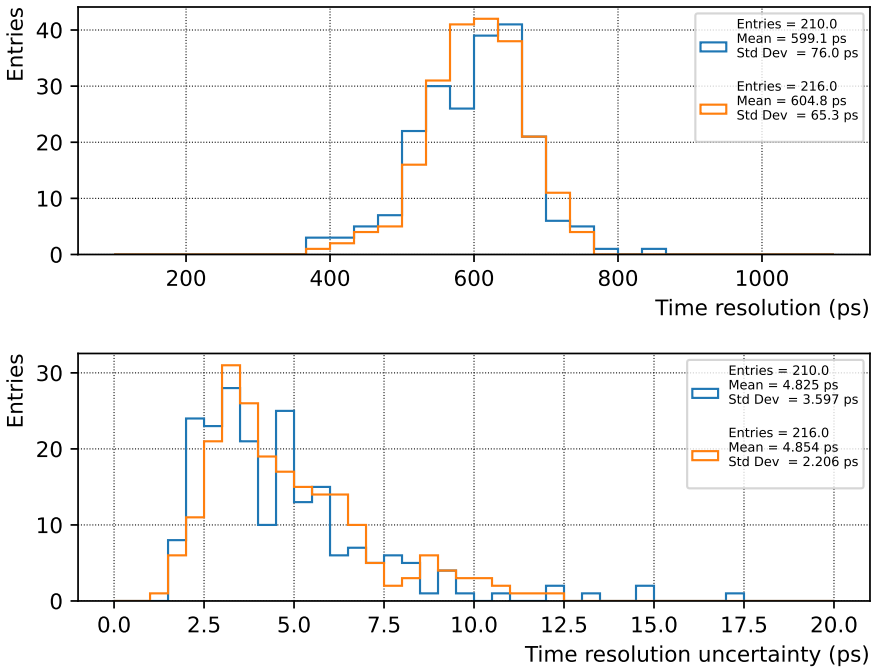

Figure 13. Time resolution of the 8-inch OMs (top) with the corresponding statistical uncertainties (bottom). The orange and blue histograms correspond to the OMs of Italian-side and French-side M-walls respectively. Reproduced from [27].

In order to provide a global time resolution of the SuperNEMO calorimeter, weighted averages have been computed for the 5- and 8-inch PMTs. Systematic studies varying the analysis cuts were

2025 JINST 20 T11003

performed to estimate the systematic uncertainties on these averaged resolutions. The final result for the time resolution of the main walls of the SuperNEMO calorimeter, extracted from the ^{60}Co data, is presented in table 1. Since the 8-inch PMTs collect more scintillation photons, the time resolution is better for these OMs compared to the 5-inch.

Table 1. Weighted average of the individual time resolutions of the SuperNEMO OMs from the calorimeter M-walls extracted from the ^{60}Co data. Reproduced from [27].

	8-inch PMTs	5-inch PMTs
Italian-side M-wall	614 ± 2 (stat) $^{+64}_{-1}$ (syst) ps	828 ± 5 (stat) $^{+101}_{-1}$ (syst) ps
French-side M-wall	619 ± 2 (stat) $^{+49}_{-4}$ (syst) ps	814 ± 6 (stat) $^{+73}_{-1}$ (syst) ps

The final time resolution of about 615 ps with γ-particles is slightly better than the 660 ps measured for NEMO-3 [29]. This result suggests that we may reach a better value than 250 ps for 1-MeV electrons in SuperNEMO, compared to NEMO-3, which is the final objective of the time analysis. The time resolutions are significantly better for electrons since they interact within the first millimeters of the scintillator's front face. We can also expect to improve the time analysis of SuperNEMO, since this work was done at an early stage of the detector commissioning, with limited statistics.

5 Energy calibration of the calorimeter

Precisely measuring the energy of the two electrons from a DBD event is of major importance for SuperNEMO, to search for $0\nu\beta\beta$ at the end of the $2\nu\beta\beta$ energy spectrum. Having the best possible energy resolution is essential for this separation. The energy calibration and its stability over time is one of the most important tasks for the experiment. The energy calibration of the SuperNEMO calorimeter will be mostly performed by regular deployment of the ^{207}Bi sources, between the $\beta\beta$ source foils in the plane of the source frame. The deployment system was already active at the time of the calorimeter commissioning, but as the activity of the sources is very low ($A < 150$ Bq [17]), it is impossible to identify the ^{207}Bi conversion electrons without the tracking detector and without shielding. Thus, another method has been used to perform the energy calibration of the calorimeter, which was inspired by [30].

5.1 Energy calibration using γ-rays

Given the importance of the energy measurement, studies of the SuperNEMO calorimeter's energy response began as soon as was possible [31], despite the inability to reconstruct electrons. Since the shielding had not yet been installed, we had an opportunity to attempt the first energy calibration of SuperNEMO's calorimeter using the external γ's emitted by the rock of the laboratory. This γ flux at LSM is dominated by decays of the ^{40}K, ^{214}Bi and ^{208}Tl isotopes. Since they have different energies, it is possible to detect several Compton edges on the total energy spectrum in each calorimeter block, providing several energy-calibration points at a time. There are almost ten γ-rays of significant intensity to consider in the ^{214}Bi decays, which cannot be identified individually, given the energy resolution of the calorimeter, but its total spectrum can still be used. The 1460 keV of ^{40}K and the 2615 keV of ^{208}Tl are, on the other hand, easily identified.

2025 JINST 20 T11003

In order to fit both the position and the rate of all these γ-rays in the energy spectrum of each OM, simulations of the three isotopes, with initial vertex positions at the walls of the LSM, were performed. This enabled the creation of *probability density functions* (PDF), which have been used to fit the measured spectra, using the RooFit library provided by ROOT [32].

Having several energies tested at the same time is also very important for SuperNEMO because several non-linearity effects have to be taken into account. These effects have been studied by the SuperNEMO collaboration, using an electron spectrometer beam [33] and precise optical simulations [34]. Three main effects can produce non-linearities in the scintillator blocks: inhomogeneities based on the location in the scintillator relative to the PMT, Birks quenching of the scintillation light [35] and the production of Cherenkov light by higher-energy charged particles. The geometrical light-collection effect dominates, because of the large volume of the scintillator blocks. It can lead to a 50 % increase for light produced just in front of the photocathode compared to the middle of the scintillator's entrance face, and a 10 % loss in the corners. Birks' law produces a few-percent increase above 1 MeV[2] but, most importantly, a loss of 10 % at 200 keV. Similarly, the Cherenkov effect can produce a 2 % increase in the collected energy above 1 MeV, and a 2 % decrease below. These effects were applied to the simulated PDFs before using them to fit the measured energy spectra of the OMs [36].

The energy spectrum of each OM can then be fitted to determine the five needed parameters: one calibration constant, one energy resolution (res) of the form $\sigma_E = \text{res} \times \sqrt{E}$, and one activity for each of the three isotopes. The two first parameters are scanned in a defined range and the activities are adjusted by the fit. A statistical χ^2 test is computed at each step of the scans and the best calibration parameters are determined by fitting the $\Delta\chi^2$ curve, to find the minimum. An example of the calibration result for one M-wall OM is presented in figure 14.

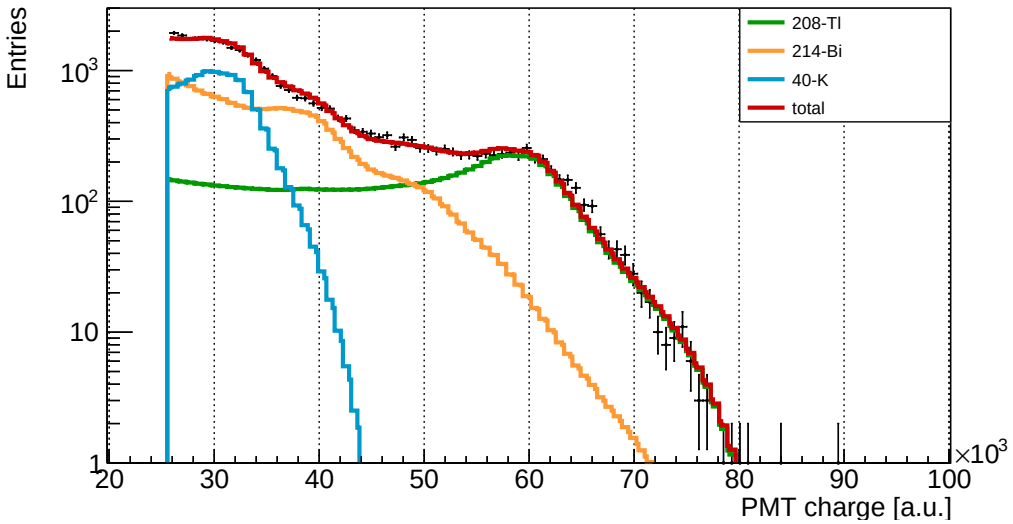

Figure 14. Example of the result of the energy calibration of the OM M-wall 1.9.9 of the SuperNEMO calorimeter. The contributions from the three external background radionuclides are represented in cyan for ^{40}K, in orange for ^{214}Bi and in green for ^{208}Tl. The red line represents the total reconstructed spectrum that gives the best agreement to the data points, shown in black [36].

[2] 1 MeV has been chosen as the reference for the normalization of the relative effects.

2025 JINST 20 T11003

5.2 Alignment of the calorimeter OMs

Almost all the optical modules have been calibrated using this new method. Figure 15 presents the current status of the energy calibration for the 8-inch OMs of the M-wall, on the amplitude and the charge spectra. A good alignment, at a level of about 7.5 %, has been obtained on the PMT pulse amplitudes (standard deviation divided by the mean of the histogram in figure 15 left), which is the relevant parameter to align trigger thresholds. Moreover, the amplitude histogram shows a low-amplitude cutoff, which is due to the requirement of having a minimal gain of 190 mV/MeV. This value was optimised in order to ensure a sufficient coverage of an energy range from 150 keV up to around 12 MeV, given the ±1.25 V dynamic range of the electronics. Nevertheless, the charge of the pulse is a better estimate of the measured energy, compared to the signal amplitude, and will be used in the event reconstruction.

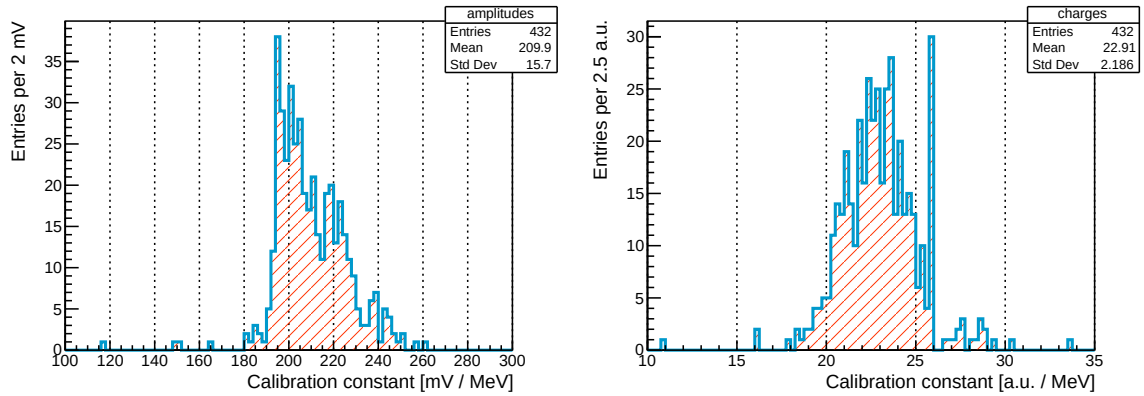

Figure 15. Distribution of the calibration constants of the M-wall OMs of the SuperNEMO calorimeter in amplitude (left) and charge (right) [36]. The calibration constants are aligned here relative to the PMT pulse amplitude, because this is the variable of interest for the trigger threshold.

This SuperNEMO energy calibration method has proven to be very powerful in determining the calibration constants of the OMs. However, no clear relationship was found between energy resolution and a minimal χ^2 for the fit of activities; a step-wise increase in the energy-resolution parameter in the model resulted in large fluctuations in the best-fit χ^2 values, with no observable trend. A dedicated study will be conducted on this crucial parameter for SuperNEMO, using precise electron tracking and energy measurement.

This work has also been used to measure the flux of the ambient γ-rays at LSM, whose result will be the subject of another publication. It will give a reference spectrum for the simulation of the external background in the SuperNEMO experiment, as well as for other experiments located in the LSM.

6 Conclusions and outlook

This article is the first SuperNEMO publication presenting an analysis of data from the SuperNEMO Demonstrator. The data were acquired at an early stage of the experiment, when the tracking detector was not yet commissioned, and the detector shielding was not yet installed. However, it was already possible to commission the SuperNEMO calorimeter with γ-particles in this configuration. We have used either calibration sources or the ambient-γ background of the LSM.

We have first reported a validation of the functioning of the 712 OMs with their signal- and high-voltage cabling, despite a few broken PMTs. The reflectometry method used for this validation also allowed us to measure the time delays between all the OMs, which will be important to detect coincidence events, like double-beta-decay.

Secondly, we have presented the use of two almost-coincident γ-rays emitted by a ^{60}Co source, to calibrate, in time, all the calorimeter OMs. This second time alignment allowed us to account for all the effects that could produce relative delays between two OMs and achieved a precision of about 120 ps. This analysis also allowed us to extract the time resolution for γ-particles, which is around 615 ps for the OMs of the SuperNEMO calorimeter M-wall.

Finally, we have performed the energy calibration of the SuperNEMO calorimeter with the ambient-γ background of the LSM, which allowed an alignment of about 7.5 %. A novel fitting method using the three natural radionuclides, ^{40}K, ^{208}Tl and ^{214}Bi, has been implemented. It also allowed us to incorporate optical corrections to reproduce the measured spectra. This improved the understanding of the detection of γ-particles in the SuperNEMO scintillator blocks.

At this stage all the functioning OMs have been aligned at in time and in energy. The calorimeter can thus be used for physics data taking, which is about to start. The tracking detector has now been commissioned and the shielding integration is almost complete. This configuration will allow us to determine crucial calorimeter parameters, such as energy and time resolutions, with electron tracks.

Acknowledgments

The authors would like to thank the staff of the LSM (Laboratoire Souterrain de Modane), Université Grenoble Alpes, Univ. Savoie Mont Blanc, Grenoble INP, CNRS, IN2P3, LPSC/LSM, 38026 Grenoble, France, for their technical assistance in assembling and operating the detector.

We also would like to thank the CC-IN2P3 computing center, Centre de Calcul de l'Institut National de Physique Nucléaire et de Physique des Particules, CNRS, IN2P3, 69627 Villeurbanne, France, providing all the resources for data transfer, storage processing and analysis.

Finally, we acknowledge support by the grants agencies of the CNRS/IN2P3 in France, Czech Republic, NSF in the U.S.A., RFBR in Russia, Slovakia and STFC in the U.K.

Finally, we acknowledge support by CNRS/IN2P3 in France, the MEYS of the Czech Republic (Contract Number LM2023063), NRFU in Ukraine (Grant No. 2023.03/0213), NSF in the U.S.A., Slovak Research and Development Agency (APVV-15-0576, APVV-21-0377) and STFC in the U.K.

References

[1] R. Arnold et al., *Technical design and performance of the NEMO 3 detector*, *Nucl. Instrum. Meth. A* **536** (2005) 79 [physics/0402115].

[2] SuperNEMO collaboration, *Probing New Physics Models of Neutrinoless Double Beta Decay with SuperNEMO*, *Eur. Phys. J. C* **70** (2010) 927 [arXiv:1005.1241].

[3] NEMO collaboration, *Measurement of the Double Beta Decay Half-life of Nd-150 and Search for Neutrinoless Decay Modes with the NEMO-3 Detector*, *Phys. Rev. C* **80** (2009) 032501 [arXiv:0810.0248].

[4] NEMO-3 collaboration, *Measurement of the two neutrino double beta decay half-life of Zr-96 with the NEMO-3 detector*, *Nucl. Phys. A* **847** (2010) 168 [arXiv:0906.2694].

2025 JINST 20 T11003

[5] NEMO-3 collaboration, *Measurement of the Double Beta Decay Half-life of ^{130}Te with the NEMO-3 Detector*, *Phys. Rev. Lett.* **107** (2011) 062504 [arXiv:1104.3716].

[6] NEMO-3 collaboration, *Measurement of the double-beta decay half-life and search for the neutrinoless double-beta decay of ^{48}Ca with the NEMO-3 detector*, *Phys. Rev. D* **93** (2016) 112008 [arXiv:1604.01710].

[7] NEMO-3 collaboration, *Measurement of the $2\nu\beta\beta$ Decay Half-Life and Search for the $0\nu\beta\beta$ Decay of ^{116}Cd with the NEMO-3 Detector*, *Phys. Rev. D* **95** (2017) 012007 [arXiv:1610.03226].

[8] R. Arnold et al., *Final results on ^{82}Se double beta decay to the ground state of ^{82}Kr from the NEMO-3 experiment*, *Eur. Phys. J. C* **78** (2018) 821 [arXiv:1806.05553].

[9] NEMO-3 collaboration, *Detailed studies of ^{100}Mo two-neutrino double beta decay in NEMO-3*, *Eur. Phys. J. C* **79** (2019) 440 [arXiv:1903.08084].

[10] F. Šimkovic, R. Dvornický, D. Stefánik and A. Faessler, *Improved description of the $2\nu\beta\beta$ -decay and a possibility to determine the effective axial-vector coupling constant*, *Phys. Rev. C* **97** (2018) 034315 [arXiv:1804.04227].

[11] NEMO collaboration, *Measurement of double beta decay of Mo-100 to excited states in the NEMO 3 experiment*, *Nucl. Phys. A* **781** (2007) 209 [hep-ex/0609058].

[12] NEMO-3 collaboration, *Search for the double-beta decay of ^{82}Se to the excited states of ^{82}Kr with NEMO-3*, *Nucl. Phys. A* **996** (2020) 121701 [arXiv:2001.06388].

[13] NEMO-3 collaboration, *Measurement of double-β decay of ^{150}Nd to the 0_1^+ excited state of ^{150}Sm in NEMO-3*, *Eur. Phys. J. C* **83** (2023) 1117 [arXiv:2203.03356].

[14] A. Jeremie and A. Remoto, *The SuperNEMO $\beta\beta$ source production*, *PoS* **ICHEP2016** (2017) 1018.

[15] X. Aguerre et al., *Fabrication of thin planar radiopure foils with ^{82}Se for the SuperNEMO Demonstrator*, arXiv:2509.08931.

[16] SuperNEMO collaboration, *The BiPo-3 detector for the measurement of ultra low natural radioactivities of thin materials*, 2017 *JINST* **12** P06002 [arXiv:1702.07176].

[17] SuperNEMO collaboration, *Measurement of the distribution of ^{207}Bi depositions on calibration sources for SuperNEMO*, 2021 *JINST* **16** T07012 [arXiv:2103.14429].

[18] R. Hodák et al., *Characterization and long-term performance of the Radon Trapping Facility operating at the Modane Underground Laboratory*, *J. Phys. G* **46** (2019) 115105.

[19] A.S. Barabash et al., *Calorimeter development for the SuperNEMO double beta decay experiment*, *Nucl. Instrum. Meth. A* **868** (2017) 98 [arXiv:1707.06823].

[20] R. Hodák et al., *Improvement of the energy resolution of the scintillating detectors for the low background measurement*, *AIP Conf. Proc.* **1672** (2015) 130003.

[21] S. Calvez, *Development of reconstruction tools and sensitivity of the SuperNEMO demonstrator*, Ph.D. thesis, Université Paris-Saclay, Paris, France (2017).

[22] D. Breton, E. Delagnes and M. Houry, *Very high dynamic range and high-sampling rate VME digitizing boards for physics experiments*, in the proceedings of the *IEEE Symposium Conference Record Nuclear Science 2004*, Rome, Italy, October 16–22 (2004) [DOI:10.1109/nssmic.2004.1462524].

[23] G. Oliviero, *Expérience SuperNEMO pour la recherche de la double désintégration bêta sans émission de neutrino: conception et réalisation du système de déclenchement du module démonstrateur*, Ph.D. thesis, Université Caen Normandie, Caen, France (2018).

2025 JINST 20 T11003

[24] D. Breton, E. Delagnes and J. Maalmi, *Using ultra fast analog memories for fast photodetector readout*, *Nucl. Instrum. Meth. A* **695** (2012) 61.

[25] H. Tedjditi, *Optimisation de la reconstruction gamma de l'expérience SuperNEMO en vue de l'étude du bruit de fond: Développement d'un détecteur sphérique proportionnel pour l'étude du radon dans l'expérience SuperNEMO*, Ph.D. thesis, Aix-Marseille Université, Marseille, France (2021).

[26] C. Girard-Carillo, *Study of ^{208}Tl background rejection influence on the $0\nu\beta\beta$ decay sensitivity, characterisation of SuperNEMO demonstrator calorimeter timing performance*, Ph.D. thesis, Université Paris-Saclay, Paris, France (2020).

[27] M. Hoballah, *Characterization of the Timing Properties of the SuperNEMO Demonstrator. Extraction of the SuperNEMO Sensitivity to the Axial-Vector Coupling Constant*, Ph.D. thesis, Université Paris-Saclay, Paris, France (2022).

[28] D. Boursette, *Neutrino physics with SoLid and SuperNEMO experiments*, Ph.D. thesis, Université Paris-Saclay, Paris, France (2018).

[29] C. Augier, *Expérience NEMO 3 — Avantages et limitations
Prospective pour la physique double bêta*, Habilitation à diriger des recherches, Université Paris Sud — Paris XI, Paris, France (2005).

[30] P. Loaiza et al., *The BiPo-3 detector*, *Appl. Radiat. Isot.* **123** (2017) 54.

[31] A. Pin, *Recherche de la nature du neutrino via la décroissance double bêta sans émission de neutrinos: Caractérisation et optimisation du calorimètre SuperNEMO et impact sur la recherche de la décroissance du 82Se: Développement du premier prototype LiquidO*, Ph.D. thesis, Université de Bordeaux, Bordeaux, France (2020).

[32] R. Brun and F. Rademakers, *ROOT — An object oriented data analysis framework*, *Nucl. Instrum. Meth. A* **389** (1997) 81.

[33] C. Marquet et al., *High energy resolution electron beam spectrometer in the MeV range*, 2015 *JINST* **10** P09008.

[34] A. Huber, *Recherche de la nature du neutrino avec le détecteur SuperNEMO: simulations optiques pour l'optimisation du calorimètre et performances attendues pour le ^{82}Se*, Ph.D. thesis, Université de Bordeaux, Bordeaux, France (2017).

[35] J.B. Birks, *The theory and practice of scintillation counting*, Pergamon (1964).

[36] X. Aguerre, *Recherche de la décroissance double bêta sans émission de neutrino du 82Se avec l'expérience SuperNEMO: reconstruction de l'énergie mesurée avec le calorimètre et analyse des premières données du démonstrateur*, Ph.D. thesis, Université de Bordeaux, Bordeaux, France (2023).

2025 JINST 20 T11003